Chinese Chemical Letters 34 (2023) 108400

Contents lists available at ScienceDirect

Chinese Chemical Letters

journal homepage: www.elsevier.com/locate/cclet

An integrated supramolecular fungicide nanoplatform based on pH-sensitive metal–organic frameworks

Chao-Yi Wang[a,b], Yu-Qing Liu[b], Chengguo Jia[b], Ming-Zhe Zhang[b], Chun-Li Song[a], Changling Xu[a], Ran Hao[a], Jian-Chun Qin[b,*], Ying-Wei Yang[a,*]

[a] College of Chemistry, Jilin University, Changchun 130012, China
[b] College of Plant Science, Jilin University, Changchun 130062, China

ARTICLE INFO

Article history:
Received 10 February 2023
Revised 18 March 2023
Accepted 28 March 2023
Available online 31 March 2023

Keywords:
Controlled release
Fungicide nanoplatform
Host-guest chemistry
Microenvironment-responsive
Supramolecular chemistry

ABSTRACT

The construction of an integrated nanoplatform with controlled fungicide delivery features in the specific microenvironment produced by fungal pathogens is a highly desirable strategy to improve the utilization of fungicides. Herein, we report a supramolecular fungicide delivery system based on benzimidazole-modified NH_2-MIL-101(Fe) metal–organic frameworks (B-MIL-101(Fe) MOFs) as carriers loaded with osthole (OS), and β-cyclodextrin (β-CD) as nanovalves to form β-CD@B-MIL-101(Fe)-OS. The nanoplatform can release the loaded OS for fungus control through self-degradation of the MOFs skeleton in an oxalic acid microenvironment produced by *Botrytis cinerea*. The experimental results exhibit that the constructed supramolecular fungicide delivery system could effectively inhibit mycelial growth and protect the tomatoes from infection by *B. cinerea* during the ripening stage. This strategy constructs a facile and integrated supramolecular drug delivery system for *B. cinerea* control and opens up a new avenue for the sustainable development of modern agriculture.

The utilization of supramolecular chemistry and nanomaterials for the construction of controlled drug delivery system offers a superior platform to solve the problems of the indiscriminate and excessive use of pesticides [1–4]. Controlled pesticide/fertilizer delivery systems have made a remarkable advance in the agricultural field through precise and efficient release of agrochemicals to reduce pesticide/fertilizer exposure to the environment [5–9]. The construction of pesticides nanoplatforms can effectively solve the problem of poor solubility and stability of pesticides [10,11], and smartly respond to different external stimuli, including light [12], temperature [13], ion [14], and ultrasound [15], to release pesticides on demand [16]. However, the fabrication of an integrated pesticides nanoplatform that can respond to the specific microenvironment related to the localized necrosis of plant disease is rarely explored in the agricultural field [11,17]. In 2021, Zhang and coworkers constructed a glucanase-responsive fungicide release system for a rice blast control [18]. In this system, mesoporous silica nanoparticles (MSNs) were used as nanocarriers loaded with chlorothalonil (CHT), and functionalized β-glucans were used as nanovalves to form CHT@MSNs-β-glucans nanoplatform, which could be triggered by the defensive β-glucanase in rice plants and the pathogenic β-glucanases in *Magnaporthe oryzae* to release fungicide. The experimental results demonstrated that the prepared nanoplatforms could effectively protect the loaded CHT from photolysis and hydrolysis, enhance the distribution time of CHT in different tissues of rice plants compared with CHT commercial product, and showed a lower toxicity to *Daphnia magna* and side effects to soil microbial communities.

Commonly, most of the pesticides loaded in the controlled delivery systems are synthetic pesticides that can protect crops from biotic and abiotic stresses, and improve the yield [19–21]. However, synthetic pesticides induce multidrug resistance in fungal pathogens, insects, and weeds [22–24], accumulate in the environment, and cause potential toxicity to biodiversity [25], which makes synthetic pesticides unsuitable for long-term application in sustainable agriculture. Therefore, the development of botanical pesticides with high efficiency and safety for crop disease control and the sustainable development of green agriculture is of great significance [26].

Osthole (OS, 7-methoxy-8-isopentenoxycoumarin), a coumarin compound isolated from the dried fruits of *Cnidium* monnieri (L.) Cusson, exhibits many biological activities, including anticancer [27], antiinflammation [28], antiallergic [29], and antiosteoporosis effects [30]. Meanwhile, OS as botanical pesticide with a small molecular size, shows excellent biological activity in controlling

* Corresponding authors.
E-mail addresses: qinjc@jlu.edu.cn (J.-C. Qin), ywyang@jlu.edu.cn (Y.-W. Yang).

https://doi.org/10.1016/j.cclet.2023.108400
1001-8417/

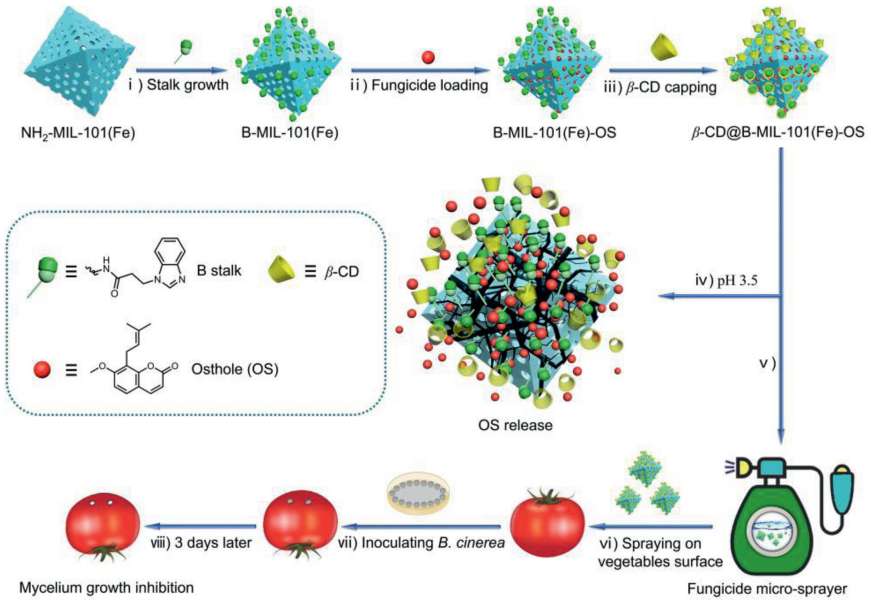

Fig. 1. Schematic description of the fabrication of the supramolecular fungicide delivery system, using B-MIL-101(Fe) as nanocarriers loaded with OS, and β-CD as nanovalves to form β-CD@B-MIL-101(Fe)-OS for *B. cinerea* control.

gray mold disease and powdery mildew [31,32], which is suitable to be loaded into a porous controlled release system.

In addition, metal–organic frameworks (MOFs), as a class of porous crystalline hybrid materials have been widely used in the adsorption/separation [33–35], catalysis [36,37], gas storage [38], chemical sensing [39,40], and drug delivery [41,42], due to their excellent physicochemical features such as facile synthesis and functionalization, flexible structure, ultrahigh porosity, large surface area and drug loading capacity, and good biocompatibility [43,44]. Among the numerous known MOFs, the MIL (MIL = Materials of Institut Lavoisier) family built from trivalent metal nodes and carboxylate linkers pioneered by Férey and coworkers has particularly drawn great attention [41,45]. Specifically, the Fe-based MOF materials, MIL-101(Fe), which weaves $FeCl_3$ precursors and terephthalic acid (H_2BDC) molecular units into octahedral frameworks, have exhibited ongoing potential for biomedical applications, especially for drug storage and release [46–48]. In 2019, Jiang, Zhang, and coworkers fabricated a smart drug delivery system based on polylactic acid and polyethylene glycol-modified MIL-101(Fe) nanovehicles for real-time imaging and chemo-photodynamic therapy [49]. In 2021, Lin, Bian, Zhu, and coworkers constructed a pH-responsive photosensitizer delivery platform, using porphyrin-modified MIL-101(Fe) for synergistic photodynamic and chemodynamic tumor therapy *via* reactive oxygen species-induced oxidation damage in the tumor microenvironment [50].

Moreover, cyclodextrin (CD), as the second-generation supramolecular macrocycle host, possesses remarkable encapsulation properties that can improve the physicochemical and/or biological characteristics of the guest molecule by host–guest interactions and is widely used in the biomedical field [51–54]. Besides, CD can also be used as nanovalves to host some molecules that are modified on the surface of the nanovehicles *via* host–guest interactions, which endows the integrated system with stimuli-responsive properties to release the loading cargo on demand, thus avoiding drug premature leakage [2,3,55].

Herein, an integrated supramolecular fungicide delivery system was constructed, using benzimidazole-modified NH_2-MIL-101(Fe) as carriers loaded with OS, and β-CD as nanovalves through the host–guest interaction between the β-CD and benzimidazole stalks (B stalks) to form β-CD@B-MIL-101(Fe)-OS that can respond to the biological stimuli associated with gray mold disease and release OS for *Botrytis cinerea* control (Fig. 1). Oxalic acid, as one of the virulence factors produced by *B. cinerea* [56], can be used as a trigger to make the skeleton of β-CD@B-MIL-101(Fe)-OS collapse, resulting in the loaded fungicides released on demand. The experimental results exhibit that the smart supramolecular fungicide delivery system could damage the structure of the mycelium and protect the tomatoes from infection by *B. cinerea* during the ripening stage, which opens up a new avenue for the protection of vegetables susceptible to *B. cinerea*.

In this study, the synthesis of NH_2-MIL-101(Fe) was according to a previous hydrothermal method, combining Fe(III)-based precursors with 2-amino-terephthalic acid (H_2ATA). After activation at 70 °C for 12 h, B stalks were attached covalently to the NH_2-MIL-101(Fe) surfaces by means of a post-synthetic amidation reaction between the carboxyl groups of 3-(1*H*-benzo[*d*]imidazol-1-yl)propanoic acid and the amino groups of NH_2-MIL-101(Fe) to achieve B-MIL-101(Fe) (Fig. S1 in Supporting information). The SEM image of NH_2-MIL-101(Fe) presented octahedral and smooth morphologies (Fig. 2A and Fig. S2A in Supporting information). After being modified with B stalks, the surface morphology of B-MIL-101(Fe) was changed compared with NH_2-MIL-101(Fe) (Fig. 2B and Fig. S2B in Supporting information). According to dynamic light scattering measurement (Fig. 2E), the average hydrodynamic diameters of NH_2-MIL-101(Fe) and B-MIL-101(Fe) were 447.8 nm and 514.8 nm, respectively, which was consistent with the crystal size *ca.* 400 nm from SME images and exhibited good dispersibility in aqueous solution. In Fig. 2F, PXRD patterns of the prepared NH_2-MIL-101(Fe) showed the crystal structure is consistent with that reported in the literature, suggesting the successful preparation of NH_2-MIL-101(Fe) [57,58]. After modification of B stalks, the prepared B-MIL-101(Fe) presented new characteristic diffraction peaks compared with NH_2-MIL-101(Fe), validating that B stalk was successfully modified onto the surface of NH_2-MIL-101(Fe). FT-IR spectrum of NH_2-MIL-101(Fe) showed that the characteristic peak at 1578 cm^{-1} is attributed to the C=N bond of NH_2-Fe-MIL-101 and the characteristic peak at 3368 cm^{-1} corresponded to the symmetrical and asymmetrical stretching vibration of amine groups in NH_2-Fe-MIL-101. After covalent functionalization with B stalks,

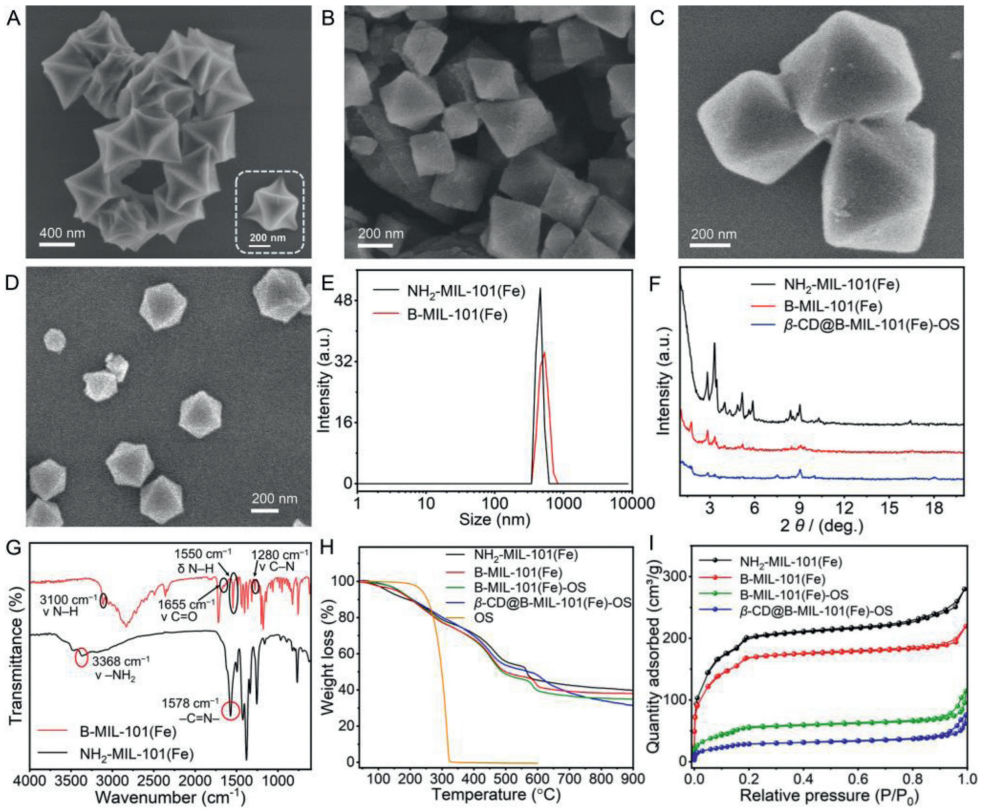

Fig. 2. Characterization of β-CD@B-MIL-101(Fe)-OS. SEM image of (A) NH_2-MIL-101(Fe), (B) B-MIL-101(Fe), (C) B-MIL-101(Fe)-OS, and (D) β-CD@B-MIL-101(Fe)-OS. (E) Average hydrodynamic diameter distribution of NH_2-MIL-101(Fe) and B-MIL-101(Fe), respectively. (F) PXRD pattern of NH_2-MIL-101(Fe), B-MIL-101(Fe), and β-CD@B-MIL-101(Fe)-OS respectively. (G) FT-IR of NH_2-MIL-101(Fe) and B-MIL-101(Fe), respectively. (H) TGA and (I) N_2 adsorption−desorption isotherms of NH_2-MIL-101(Fe), B-MIL-101(Fe), B-MIL-101(Fe)-OS and β-CD@B-MIL-101(Fe)-OS, respectively.

a new absorption peak was found at 3100 cm^{-1} (amide I band), which was attributed to the stretching vibration of N-H of the secondary amide groups in B-MIL-101(Fe), belonging to the frequency doubling peak of N-H (1550 cm^{-1}, amide II band) bending vibration. Moreover, the characteristic peak at 1280 cm^{-1} was assigned to the stretching vibration of C-N (amide III band), and the peak at 1655 cm^{-1} corresponded to the vibration of N=C in B-MIL-101(Fe), indicating the successful modification of B stalks on NH_2-MIL-101(Fe) (Fig. 2G). Furthermore, the TGA was used to study the decomposition behaviors and thermal stability of the nanoplatforms. As seen from the TGA curves, the weight loss of NH_2-MIL-101(Fe) and B-MIL-101(Fe) below 100 °C was attributed to the physical adsorption of water in both materials, and the decomposition of organic ligands in the structures was between 100 °C and 600 °C. The weight loss of B stalk was about 8.2% in the range of 110 °C to 210 °C (Fig. 2H). After OS loading, the TGA curve of B-MIL-101(Fe)-OS showed that the weight loss of OS was 13.3% between 450 °C and 570 °C, due to the decomposition of OS. The TGA curve of β-CD@B-MIL-101(Fe)-OS demonstrated that the weight loss of β-CD was 18.6% between 570 °C and 900 °C. Although it is difficult to determine the exact initial decomposition temperature of OS in β-CD@B-MIL-101(Fe)-OS, the decomposition temperature shift to a higher temperature direction, indicating enhanced thermal stability of OS loaded in the nanoplatforms. The surface zeta potential value of NH_2-MIL-101(Fe) in deionized water changed from +33.98 mV to +20.06 mV after modification of B stalks and eventually turned to +25.14 mV after loading of OS and immobilization of β-CD on the surface (Fig. S2C in Supporting information). The type I N_2 adsorptiondesorption isotherm indicated the micropore nature of B-MIL-101(Fe) and the corresponding Brunauer-Emmett-Teller (BET) surface area and Barett–Joyner–Halenda (BJH) pore size distribution were measured to be 559.0 m^2/g and 1.9 nm (Fig. 2I), respectively, indicating a great cargo loading capacity of B-MIL-101(Fe). OS with a molecule size of 0.95 nm in length (Fig. S3A in Supporting information) could be easily loaded into B-MIL-101(Fe) *via* physical mixing to form B-MIL-101(Fe)-OS (Fig. 2C) followed by the significant decrease of BET surface (199.1 m^2/g) and pore volume, and a slight effect of pore diameter (Fig. S4 and Table S1 in Supporting information). To overcome the premature release of OS during post-processing, β-CD as nanovalves were introduced onto the surface of B-MIL-101(Fe)-OS *via* hostguest interactions between the B stalk and the cavity of β-CD to form β-CD@B-MIL-101(Fe)-OS nanoplatform (Fig. 2D). According to the published literature, *N*-methylbenzimidazole stalks with the pK_a value of 5.67 that modified covalently on the surfaces of mesoporous silica nanoparticles could be encircled by the β-CD ring *via* supramolecular interactions at pH 7.4, and release the β-CD ring at pH $<$ 6 due to the protonation of the aromatic amines [59]. The related host–guest association between β-CD and 1-methylbenzimidazole was investigated *via* ^{1}H NMR spectroscopy of β-CD, 1-methylbenzimidazole, and the equimolar mixture of β-CD and 1-methylbenzimidazole in D_2O (Figs. S5 and S6 in Supporting information). As shown in Fig. S6, after the addition of β-CD, the alkyl protons signals of the benzene ring in 1-methylbenzimidazole displayed an obvious upfield shift in comparison with pure 1-methylbenzimidazole due to the shielding effect of β-CD, indicating the existence of host–guest interaction between β-CD and 1-methylbenzimidazole. The stoichiometry of the host–guest binding mode between β-CD and 1-methylbenzimidazole was 1:1 according to published literature [59,60].

According to the previous research, the MIL-101(Fe)-based MOFs materials will gradually degrade in an acidic aqueous so-

lution [49,61]. As the pH value of the oxalic acid secreted by *B. cinerea* was about 3.5 [13], the self-degradation features of β-CD@B-MIL-101(Fe)-OS in the microenvironment of plant lesion infected by *B. cinere*a was further studied. The SEM images showed that compared with the control group (Fig. S7A in Supporting information), the surface of β-CD@B-MIL-101(Fe)-OS became rough after treatment with the oxalic acid secreted by *B. cinerea* for 5 min (Fig. S7B in Supporting information), followed by the appearance of cracks and holes (Figs. S7C and D in Supporting information). The corresponding PXRD patterns verified that β-CD@B-MIL-101(Fe)-OS presented an amorphous structure after treatment with the oxalic acid secretion for 5 min (Fig. S8 in Supporting information). Based on the above experimental results, β-CD@B-MIL-101(Fe)-OS could respond to the acidic microenvironment created by *B. cinerea*, resulting in the self-degradation of MOF skeleton.

To verify that β-CD played a significant role in the drug loading capacity of β-CD@B-MIL-101(Fe)-OS, the loading amount of OS in the supramolecular fungicide nanoplatform with or without β-CD was studied and calculated to be 137.0 mg/g and 99.3 mg/g, respectively, according to LambertBeer law (Figs. S3B and C in Supporting information), which could effectively block the loss of the loaded fungicide during post-processing through host–guest interaction between β-CD and B stalks.

Subsequently, to determine the stimuli-responsive release behavior of OS from β-CD@B-MIL-101(Fe)-OS, β-CD@B-MIL-101(Fe)-OS were immersed in oxalic acid PBES (pH 3.5 and 7.4, respectively) and the amount of the released OS was monitored at different time intervals by UV-vis spectroscopy. After 48 h of treatment, the cumulative release of OS from β-CD@B-MIL-101(Fe)-OS was 28.3% at pH 7.4. In comparison, 67.6% OS was released at pH 3.5 (Fig. S9A in Supporting information), due to the self-degradation of β-CD@B-MIL-101(Fe)-OS, resulting in a fast release of OS in the acidic environment (Fig. S9B in Supporting information) [59,62]. The release behavior of OS from β-CD@B-MIL-101(Fe)-OS at different pH values indicated that β-CD@B-MIL-101(Fe)-OS featured pH-induced drug delivery properties, which confers the nanoplatform with the capability to self-degradation and release pesticides on demand in the acidic environment associated with the localized necrosis of plant disease.

The antifungal activity of β-CD@B-MIL-101(Fe)-OS against *B. cinerea* was investigated using the mycelium growth rate method and the concentration was set at 10 μg/mL and 20 μg/mL. For comparison, the antifungal activity of OS and β-CD@B-MIL-101(Fe) was also assessed under the same concentration. The images of the colony diameter on the medium of each treatment group against *B. cinerea* from the 1st day to the 4th day were shown in Fig. 3A, and the average colony diameter and the inhibition rate of different treatment groups were summarized in Table S2 in Supporting information (β-CD@B-MIL-101(Fe)-OS-10 and β-CD@B-MIL-101(Fe)-OS-20 represent the fungicide nanoplatform containing OS at the corresponding concentrations). As seen from the grown colonies, the colony diameter of β-CD@B-MIL-101(Fe)-OS groups was slightly larger than OS groups on the 2nd day because it needed time for OS to be released from the nanoplatforms, leading to a lower initial concentration of OS in the PDA media and a little lower antifungal activity (Figs. 3A and B). While for OS, the inhibition rate at the concentration of 10 μg/mL and 20 μg/mL was 46.35% and 63.03%, respectively, on the 4th day. In contrast, the inhibition rate of β-CD@B-MIL-101(Fe)-OS was 51.25% and 70.45%, respectively, under the same condition, indicating that the fungicidal activity of β-CD@B-MIL-101(Fe)-OS was better than that of OS (Figs. S10A and B in Supporting information). Due to the benzimidazole terminal of B stalk, β-CD@B-MIL-101(Fe) without OS loading also exhibited fungicidal activity against *B. cinerea*, improving the fungicidal activity of β-CD@B-MIL-101(Fe)-OS. Subsequently, we continued to monitor the colony growth of OS and β-CD@B-MIL-101(Fe)-OS groups. The fungicidal activity of β-CD@B-MIL-101(Fe)-OS at the concentration of 20 μg/mL was 32.28% on the 8th day, which was higher than that of OS groups, demonstrating a long-term fungicidal activity against *B. cinerea* (Fig. S10C in Supporting information). Moreover, according to the BB colorimetric method in our reported literature [13], the pH value of the PDA medium was close to 3.5 after *B. cinerea* was inoculated on the medium after 36 h (Fig. S10D in Supporting information). Therefore, with the oxalic acid secreted by *B. cinerea* gradually immersed into the PDA medium, the skeleton structure of β-CD@B-MIL-101(Fe)-OS will collapse, resulting in the release of OS and presenting a better inhibition effect on the growth of *B. cinerea*.

In addition, the mycelial biomass method was employed to further examine the antifungal activity of the fungicide nanoplatform against *B. cinerea* by measuring the dry weight of the fungus cake incubating in the CM containing OS, β-CD@B-MIL-101(Fe), and β-CD@B-MIL-101(Fe)-OS, respectively, for 3 days. The average biomass and the inhibition rate of each treatment group were summarized in Table S3 (Supporting information). As shown in Fig. S11 (Supporting information), the mycelial pellet volume was significantly inhibited in OS and β-CD@B-MIL-101(Fe)-OS groups in comparison with the control group on the 3rd day, and the inhibition rate of β-CD@B-MIL-101(Fe)-OS at the concentration of 10 μg/mL and 20 μg/mL reached 61.06% and 73.86%, respectively (Figs. S12A and B in Supporting information). Therefore, the above results suggested that β-CD@B-MIL-101(Fe)-OS could effectively inhibit the growth of *B. cinerea* both in solid and liquid media.

Next, the morphological structure of the mycelium treated with β-CD@B-MIL-101(Fe)-OS (20 μg/mL) was observed by SEM (Fig. 3C). SEM images indicated the mycelial structure was gradually rough and irregular after being treated with β-CD@B-MIL-101(Fe)-OS for 6 h (Fig. 3C2), and even presented malformed and morphological deformities after treated for 12 h (Fig. 3C3), compared with the fine and regular mycelial structure incubated in CM (Fig. 3C1). The experimental results showed that the as-prepared fungicide nanoplatform could damage the mycelial structure of *B. cinerea* and inhibit its normal growth. In addition, the fluorescent microscope was used to further evaluate the damage of the mycelium after being treated with β-CD@B-MIL-101(Fe)-OS (20 μg/mL) for 6 h using PI solution that can only penetrate the impaired mycelium membrane and stained cell nucleus into red [63]. The mycelium treated with OS (20 μg/mL) and β-CD@B-MIL-101(Fe) (20 μg/mL) was also tested by PI solution for comparison. After being incubated with PI solution at room temperature for 20 min, the mycelium of β-CD@B-MIL-101(Fe)-OS and OS groups was observed by fluorescence microscope under 530–550 nm of excitation wavelengths and exhibited red fluorescence compared with control and β-CD@B-MIL-101(Fe) groups (Fig. 3D and Figs. S13A-F in Supporting information). The fluorescence images revealed that the OS could effectively release from β-CD@B-MIL-101(Fe)-OS, damaging the mycelium structure.

Inspired by the effective inhibition effect of β-CD@B-MIL-101(Fe)-OS on *B. cinerea in vitro*, the antifungal activity of β-CD@B-MIL-101(Fe)-OS was further investigated using susceptible vegetables to *B. cinerea*. Tomato, as an essential cash crop susceptible to *B. cinerea*, was selected as a model vegetable to explore the feasibility of β-CD@B-MIL-101(Fe)-OS as fungicide nanoplatforms for vegetable protection against *B. cinerea* [56]. After being treated with β-CD@B-MIL-101(Fe)-OS (100 μg/mL) for 1 h, the fungus cakes (5 mm in diameter) of *B. cinerea* were inoculated on two different positions of each tomato surface to avoid the sensitivity difference of different parts of each tomato. After incubation for 96 h, a large soft rot area was visualized on the surface of the tomatoes in the control group. In comparison, the tomatoes treated with β-CD@B-MIL-101(Fe)-OS showed no soft rot, demonstrating that β-CD@B-MIL-101(Fe)-OS could effectively inhibit the mycelial

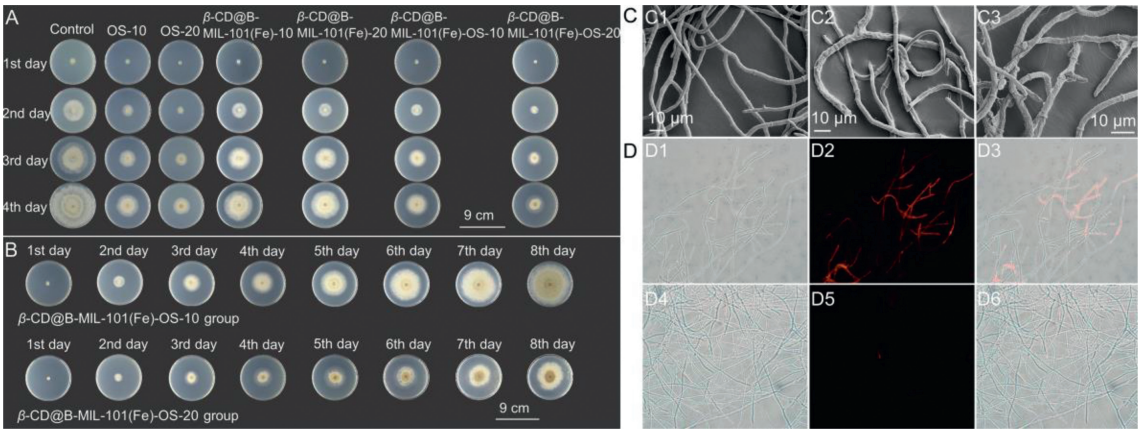

Fig. 3. (A) *In vitro* antifungal activity of OS, β-CD@B-MIL-101(Fe), and β-CD@B-MIL-101(Fe)-OS against *B. cinerea* at the corresponding concentrations and control group from the 1st day to the 4th day. (B) Antifungal activity of β-CD@B-MIL-101(Fe)-OS against *B. cinerea* at the corresponding concentrations from the 1st day to the 8th day. (C) SEM images of the mycelia incubated in CM for 84 h (C1), treated with β-CD@B-MIL-101(Fe)-OS (20 μg/mL) for 6 h (C2), and (C3) for 12 h. (D) Fluorescence images (10×20 times scope) of mycelia treated with β-CD@B-MIL-101(Fe)-OS (20 μg/mL) for 12 h and stained with the PI solution under (D1) bright field, (D2) dark field, and (D3) the merged image of (D1) and (D2). Fluorescence images of mycelium in the control group stained with PI solution under (D4) bright field, (D5) dark field, and (D6) the merged image of (D4) and (D5).

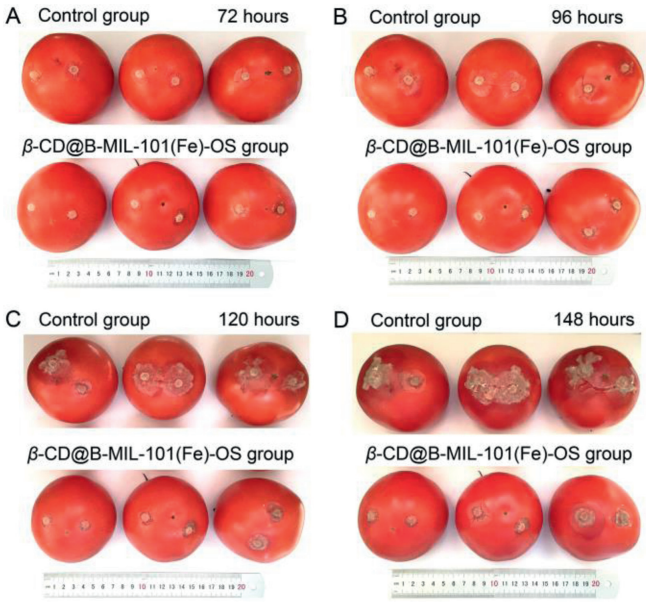

Fig. 4. Protective effect of β-CD@B-MIL-101(Fe)-OS on tomato. Images of tomatoes treated with β-CD@B-MIL-101(Fe)-OS at 100 μg/mL and control group inoculated with the fungus cake (5 mm in diameter) of *B. cinerea* for (A) 72, (B) 96, (C) 120, and (D) 148 h.

growth of *B. cinerea* and protect tomatoes from *B. cinerea* infection during the ripening stage (Fig. 4). In addition, different from the tomato tissues (pH 6), the pH value of the localized necrotic area of tomatoes infected with *B. cinerea* was about 3.5 measured with precision and wide pH test paper, respectively, which was favorable to autonomous release OS from β-CD@B-MIL-101(Fe)-OS (Figs. S14A and B in Supporting information), and significantly improve the utilization efficiency of fungicides, reduce the adverse impact of fungicides on crops and the environment.

In this work, an integrated supramolecular fungicide delivery system was successfully designed and constructed, using B-MIL-101(Fe) as carriers loaded with OS, and β-CD as nanovalves to form β-CD@B-MIL-101(Fe)-OS, which can respond to the oxalic acid associated with gray mold disease and release OS on demand for *B. cinerea* control. The experimental results showed that the constructed supramolecular fungicide delivery system could release OS in a controlled fashion, effectively inhibit mycelial growth *via* damage to the structure of mycelia, and protect the tomatoes from infection by *B. cinerea*. This strategy of constructing a facile and autonomous activation supramolecular drug delivery system dramatically improves fungicide utilization efficiency, reduces the adverse impact of synthetic fungicides on crops and the environment, and opens up a powerful avenue for the development of modern sustainable agriculture.

Declaration of competing interest

The authors declare that they have no known competing financial interests or personal relationships that could have appeared to influence the work reported in this paper.

Acknowledgments

This work was supported by the National Natural Science Foundation of China (Nos. 52173200, 31470414, 31870332), the Natural Science Foundation of Jilin Province (No. 20230101052JC), the Special Fund Project of Shenzhen City for Local Science and Technology Development Guided by the Central Government (No. 2021Szvup049), the National Major Increase or Decrease Project-Construction of the sustainable utilization capacity of famous traditional Chinese medicine resources (No. 2060302), and the Fundamental Research Funds for the Central Universities (No. 2022-JCXK-13).

Supplementary materials

Supplementary material associated with this article can be found, in the online version, at doi:10.1016/j.cclet.2023.108400.

References

[1] Macmillan, Nature 286 (1980) 832.
[2] A.E. Kaziem, Y. Gao, S. He, J. Li, J. Agric. Food Chem. 65 (2017) 7854–7864.
[3] A.E. Kaziem, Y. Gao, Y. Zhang, et al., J. Hazard. Mater. 359 (2018) 213–221.
[4] X. Zhang, Q. Huang, Z.Z. Zhao, et al., J. Agric. Food Chem. 67 (2019) 7783–7792.
[5] S. Song, Y. Wang, J. Xie, et al., ACS Appl. Mater. Interfaces 11 (2019) 34258–34267.
[6] D.W. Sun, L. Huang, H. Pu, J. Ma, Chem. Soc. Rev. 50 (2021) 1070–1110.
[7] C.Y. Wang, J. Yang, J.C. Qin, Y.W. Yang, Adv. Sci. 8 (2021) 2004525.
[8] P. Vejan, T. Khadiran, R. Abdullah, N. Ahmad, J. Control. Release 339 (2021) 321–334.
[9] H. Lu, C. Dun, H. Jariwala, et al., J. Control. Release 350 (2022) 748–760.

[10] M.B. Cadena, G.M. Preston, R.A.L. Van der Hoorn, H.E. Townley, I.P. Thompson, Ind. Crops Prod. 122 (2018) 582–590.
[11] S. Yan, Q. Hu, Q. Jiang, et al., ACS Appl. Mater. Interfaces 13 (2021) 36350–36360.
[12] C. Gao, Q. Huang, Q. Lan, et al., Nat. Commun. 9 (2018) 2967.
[13] C.Y. Wang, X.Y. Lou, Z. Cai, et al., ACS Appl. Mater. Interfaces 13 (2021) 32295–32306.
[14] G. Zhang, L. Zhou, D. Cai, Z. Wu, Carbon 129 (2018) 711–719.
[15] X. Li, J. Han, X. Wang, et al., Mater. Chem. Front. 3 (2019) 103–110.
[16] M. Bruneau, S. Bennici, J. Brendle, et al., J. Control. Release 294 (2019) 355–371.
[17] S. Ribes, M. Ruiz-Rico, É. Pérez-Esteve, et al., Food Control 81 (2017) 181–188.
[18] A.E. Kaziem, L. Yang, Y. Lin, et al., ACS Sustain. Chem. Eng. 9 (2021) 9126–9138.
[19] X. Zhang, X. Tang, C. Zhao, et al., Chem. Eng. J. 431 (2022) 133351.
[20] B. Zhang, G. Yu, J. Li, et al., Int. J. Biol. Macromol. 153 (2020) 17–25.
[21] A. Zou, Y. Yang, J. Cheng, V.M. Garamus, N. Li, J. Agric. Food Chem. 66 (2018) 6262–6268.
[22] P. Leroux, R. Fritz, D. Debieu, et al., Pest Manage. Sci. 58 (2002) 876–888.
[23] V. Balabanidou, L. Grigoraki, J. Vontas, Curr. Opin. Insect Sci. 27 (2018) 68–74.
[24] C. Surridge, Nat. Plants 3 (2017) 16217.
[25] W. Mischko, M. Hirte, S. Roehrer, et al., Green Chem. 20 (2018) 2637–2650.
[26] Y. Zhang, B. Liu, K. Huang, et al., ACS Appl. Mater. Interfaces 12 (2020) 37607–37618.
[27] L. Liu, J. Mao, Q. Wang, et al., Biomed. Pharmacother. 94 (2017) 1020–1027.
[28] P.C. Liao, S.C. Chien, C.L. Ho, et al., J. Agric. Food Chem. 58 (2010) 10445–10451.
[29] P.R. Chiu, W.T. Lee, Y.T. Chu, et al., Pediatr. Neonatol. 49 (2008) 135–140.
[30] P.L. Kuo, Y.L. Hsu, C.H. Chang, J.K. Chang, J. Pharmacol. Exp. Ther. 314 (2005) 1290–1299.
[31] Q.Q. Wang, S.G. Zhang, J. Jiao, P. Dai, W.H. Zhang, Molecules 26 (2021) 372.
[32] Z. Shi, F. Wang, W. Zhou, P. Zhang, Y.J. Fan, Int. J. Mol. Sci. 8 (2007) 1001–1012.
[33] R.J. Drout, L. Robison, Z. Chen, T. Islamoglu, O.K. Farha, Trends Chem. 1 (2019) 304–317.
[34] X. Zhang, Y. Yang, P. Qin, et al., Chin. Chem. Lett. 33 (2022) 903–906.
[35] Y.P. Xia, C.X. Wang, M.H. Yu, X.H. Bu, Chin. Chem. Lett. 32 (2021) 1153–1156.
[36] H. Furukawa, E. Cordova Kyle, M. O'Keeffe, M. Yaghi Omar, Science 341 (2013) 1230444.
[37] H. Zheng, Y. Hou, S. Li, J. Ma, J. Nan, T. Li, Chin. Chem. Lett. 33 (2022) 5013–5022.
[38] O.K. Farha, A. Özgür Yazaydın, I. Eryazici, et al., Nat. Chem. 2 (2010) 944–948.
[39] D. Liu, K. Lu, C. Poon, W. Lin, Inorg. Chem. 53 (2014) 1916–1924.
[40] H. Wang, X.L. Wang, R.M. Kong, L. Xia, F.L. Qu, Chin. Chem. Lett. 32 (2021) 198–202.
[41] K.M.L. Taylor-Pashow, J. Della Rocca, Z. Xie, S. Tran, W. Lin, J. Am. Chem. Soc. 131 (2009) 14261–14263.
[42] X. Ma, Q. Wu, L. Tan, et al., Chin. Chem. Lett. 33 (2022) 1604–1608.
[43] R. Fang, A. Dhakshinamoorthy, Y. Li, H. Garcia, Chem. Soc. Rev. 49 (2020) 3638–3687.
[44] R.J. Drout, S. Kato, H. Chen, et al., J. Am. Chem. Soc. 142 (2020) 12357–12366.
[45] G. Férey, C. Mellot-Draznieks, C. Serre, F. Millange, Acc. Chem. Res. 38 (2005) 217–225.
[46] Z. Dong, Y. Sun, J. Chu, X. Zhang, H. Deng, J. Am. Chem. Soc. 139 (2017) 14209–14216.
[47] J. Della Rocca, D. Liu, W. Lin, Acc. Chem. Res. 44 (2011) 957–968.
[48] P. Horcajada, T. Chalati, C. Serre, et al., Nat. Mater. 9 (2010) 172–178.
[49] C. Wang, X. Jia, W. Zhen, M. Zhang, X. Jiang, ACS Biomater. Sci. Eng. 5 (2019) 4435–4441.
[50] J. Chen, Y. Wang, H. Niu, et al., ACS Appl. Mater. Interfaces 13 (2021) 45201–45213.
[51] H. Zheng, C. Yuan, J. Cai, et al., J. Nanobiotechnol. 20 (2022) 134.
[52] S. Qi, H. Zhang, X. Zhang, et al., Sci. Bull. 67 (2022) 1898–1909.
[53] Y. Liu, M. Hou, Z. Pan, et al., J. Nanobiotechnol. 20 (2022) 303.
[54] K. Yang, S. Qi, X. Yu, et al., Angew. Chem. Int. Ed. 61 (2022) e202203786.
[55] J. Tan, N. Meng, Y. Fan, et al., Mater. Sci. Eng. C 61 (2016) 681–687.
[56] B. Williamson, B. Tudzynsk, P. Tudzynski, J.A.L. Van Kan, Mol. Plant Pathol. 8 (2007) 561–580.
[57] D. Lupu, O. Ardelean, G. Blanita, et al., Int. J. Hydrogen Energy 36 (2011) 3586–3592.
[58] D. Wang, R. Huang, W. Liu, D. Sun, Z. Li, ACS Catal. 4 (2014) 4254–4260.
[59] H.A. Meng, M. Xue, T.A. Xia, et al., J. Am. Chem. Soc. 132 (2010) 12690–12697.
[60] H.J. Schneider, F. Hacket, V. Rüdiger, H. Ikeda, Chem. Rev. 98 (1998) 1755–1786.
[61] Y. Liu, C.S. Gong, Y. Dai, et al., Biomaterials 218 (2019) 119365.
[62] X.G. Wang, Z.Y. Dong, H. Cheng, et al., Nanoscale 7 (2015) 16061–16070.
[63] E. Dolezalova, P. Lukes, Bioelectrochemistry 103 (2015) 7–14.